Research Article | Vol. 12, No. 9 / 1 Sep 2021 / Biomedical Optics Express 5829
Biomedical Optics EXPRESS

Influence of hematoxylin and eosin staining on the quantitative analysis of second harmonic generation imaging of fixed tissue sections

RADU HRISTU,[1] STEFAN G. STANCIU,[1] ADRIAN DUMITRU,[2] BOGDAN PAUN,[3] IUSTIN FLOROIU,[1] MARIANA COSTACHE,[2] AND GEORGE A. STANCIU[1,*]

[1] *Center for Microcopy-Microanalysis and Information Processing, University Politehnica of Bucharest, 060042 Bucharest, Romania*
[2] *Department of Pathology, Carol Davila University of Medicine and Pharmacy, 050474 Bucharest, Romania*
[3] *Faculty of Automation and Computer Science, Technical University of Cluj-Napoca, 40002 Cluj-Napoca, Romania*
[*] *stanciu@physics.pub.ro*

Abstract: Second harmonic generation (SHG) microscopy has emerged over the past two decades as a powerful tool for tissue characterization and diagnostics. Its main applications in medicine are related to mapping the collagen architecture of in-vivo, ex-vivo and fixed tissues based on endogenous contrast. In this work we present how H&E staining of excised and fixed tissues influences the extraction and use of image parameters specific to polarization-resolved SHG (PSHG) microscopy, which are known to provide quantitative information on the collagen structure and organization. We employ a theoretical collagen model for fitting the experimental PSHG datasets to obtain the second order susceptibility tensor elements ratios and the fitting efficiency. Furthermore, the second harmonic intensity acquired under circular polarization is investigated. The evolution of these parameters in both forward- and backward-collected SHG are computed for both H&E-stained and unstained tissue sections. Consistent modifications are observed between the two cases in terms of the fitting efficiency and the second harmonic intensity. This suggests that similar quantitative analysis workflows applied to PSHG images collected on stained and unstained tissues could yield different results, and hence affect the diagnostic accuracy.

1. Introduction

Bright-field microscopy (BM) of hematoxylin and eosin (H&E) stained tissue sections represents at the time being the gold standard of traditional histopathology workflows aimed at tissue characterization and diagnostics. The popularity of H&E staining derives from the simplicity of the tissue preparation protocol and this stain's ability to highlight relevant pathological features in thin tissue sections. The first step in preparing tissues for such histopathology sessions involves the deparaffinization and rehydration of tissue sections obtained from paraffin embedded tissue blocks with a microtome. This step is followed by the actual staining process [1], which first involves dipping the tissue section in hematoxylin which stains nucleic acids in a blue-purple color. The tissue is then counterstained with eosin which marks proteins nonspecifically within the cytoplasm, borders of the cell membrane, red blood cells and extracellular structures (including collagen) in varying degrees of pink. Bright-field microscopy of the so prepared samples allows a trained pathologist to identify meaningful pathological features for placing a diagnostic.

Although BM of stained tissue sections represent the gold standard for tissue characterization, other imaging techniques have gained massive momentum over the past years, having huge

#428701 https://doi.org/10.1364/BOE.428701
Journal © 2021 Received 30 Apr 2021; revised 20 Jul 2021; accepted 20 Jul 2021; published 25 Aug 2021

Biomedical Optics EXPRESS

potential to overcome some of the most prominent limitations of traditional histopathology workflows. Multiphoton microscopy (MPM) [2] has emerged as a powerful method for the label-free characterization of the morphology and composition of in-vivo [3,4], ex-vivo [5–7] and fixed tissues [8]. Among the available MPM techniques, two-photon excitation fluorescence (TPEF) microscopy and second harmonic generation (SHG) microscopy have demonstrated their usefulness in probing tissue properties with important roles for establishing the tissue state and, finally, a diagnostic. TPEF involves the simultaneous absorption of two photons with combined energy sufficient to induce an electronic transition to an excited state [9]. Tissue imaging with TPEF is usually performed based on endogenous contrast, exploiting the emission of various fluorescent molecules natively present in mammalian tissues such as melanin [10], reduced nicotinamide adenine dinucleotide (NADH) and flavin adenine dinucleotide (FAD) [11]. Second harmonic generation is a coherent second order nonlinear effect in which two photons interact simultaneously with a non-centrosymmetric molecule and produce a new photon with exactly twice the energy of the interacting photons. Upon excitation with an intense short laser pulse, three types of biomolecules are known to generate second harmonic (SH) signals: tubulin [12], myosin [13] and collagen [14]. Polarization-resolved SHG (PSHG), an extension of SHG microscopy, exploits the coherent nature of the SH signals, whose intensity depends on the input laser beam polarization and on the structure and organization of the non-centrosymmetric molecules in the focal volume [15]. PSHG augments thus SHG microscopy by using theoretical models for collagen (e.g., the single-axis molecule model [16], the generic model [17]) and fitting algorithms resulting in a pixel-level quantitative analysis [18]. Ratios of the elements of the second order nonlinear susceptibility tensor ($\chi^{(2)}$) for collagen [18,19], the fitting efficiency [20] and SHG pixel intensities [21] are just a few image quantitative parameters used to characterize collagen in PSHG datasets.

Numerous results obtained throughout the past two decades have shown that SHG microscopy provides an extended insight into the collagen distribution in the extracellular matrix of different organs, which can enhance the results obtained by using traditional H&E staining. This technique is thus regarded as a powerful diagnostic tool with potential for enabling a wide variety of medical applications that can benefit from probing the collagen architecture in tissue with high precision. For different pathologies of the skin [22], breast [23,24] ovaries [24,25], thyroid [21,26], pancreas [27,28], the gastrointestinal tract [29,30], or various oral tissues [31], SHG imaging was successfully used to perform both subjective, and more importantly, quantitative analyses over the collagen distribution with massive implications for in-vivo and ex-vivo diagnostics of unstained tissues.

Many of the SHG imaging experiments performed to date have been implemented on freshly excised tissue samples [29] which is of great interest to clinical applications since it enables tissue evaluation under conditions close to the physiological ones, avoiding time-consuming preparation methods. SHG microscopy was also performed on cryosections [32], but the limiting factor is the formation of ice crystals which enables morphological distortions within the tissue. Tissue sections preparation via fixation, paraffin embedding, and microtome slicing maintains the overall tissue morphology with the advantage of prolonged storage of the tissue. Following the entire histological protocol, the tissue sections are stained with H&E. Many SHG imaging experiments were performed on both stained [33–35] and unstained [36–38] fixed tissue sections. Usually, SHG images are first recorded on the unstained section which is then stained with H&E for standard histological examination with a bright-field microscope. In such workflows, care needs to be taken for avoiding thermal modification of the tissue under intense laser pulses required by SHG imaging. It was also shown that SHG imaging can be performed on H&E de-stained tissue sections [39]. The advantage of imaging tissue sections resides in the fact that SHG microscopy can provide additional diagnostic cues to the standard histology protocol and can be applied on the same sections to complement BM observations. Furthermore, the availability of a traditional

Biomedical Optics EXPRESS

H&E image next to a SHG image, consistently facilitates the interpretation of the latter by a trained expert.

Digital pathology has largely evolved over the past years, and in connected endeavors the development of different quantitative analysis algorithms aimed at feature segmentation and identification, or classification of different tissue pathologies has gained important interest. Many such methods have also been reported to date in connection with SHG, quantitative SHG analysis being regarded as an important additional source of information to the qualitative morphological analyses carried out on intensity based SHG or BM images. However, to the best of our knowledge, past quantitative analyses of SHG datasets have not considered if the fixed tissues targeted by the experiment were stained or not, as it is largely acknowledged that H&E staining does not interfere with the observation of morphological features in SHG images based on endogenous contrast.

In this work we explore whether H&E staining influences the outputs of typical quantitative analyses of PSHG imaging. We focus on the problem of extracting specific image parameters from PSHG image stacks, in the intention to observe if the same image analysis workflow can be applied to both stained and unstained tissues to result in the same output. Our results show that addressing stained and unstained tissues with identical PSHG image analysis workflows yield different results in some scenarios, which to the best of our knowledge has not been reported to date. We consider this finding to be important as improper use of image analysis methods can affect the diagnostic accuracy, with implications for the adopted therapies and survival rates. Furthermore, our results suggest the need for novel PSHG image analysis methods and workflows that are specifically dedicated to stained or unstained tissues, and of PSHG image analysis methods that are capable to generalize better than current ones.

2. Materials and methods

2.1. The nonlinear optical microscope

Imaging of histological sections was performed with a three-channel Leica TCS SP (Leica Microsystems, Wetzlar, Germany) laser scanning confocal microscope adapted for nonlinear imaging. SHG and TPEF were measured simultaneously: SHG was collected in both forward and backward directions, while epidetection was used for TPEF. A Ti:Sapphire laser (Chameleon Ultra II, Coherent, Santa Clara, California, US) was used for nonlinear excitation. The laser provided ~140 fs pulses emitting at 870 nm with a pulse repetition rate of 80 MHz. A 40X 0.75 numerical aperture (NA) objective was used for excitation. A shortpass filter (FF01-750/SP-25, Semrock, Rochester, New York) combined with a bandpass filter (FB430-10, Thorlabs, Newton, New Jersey, United States) were used in the forward detection direction for filtering the forward-generated SHG (FSHG) collected by using a 0.9 NA condenser lens. The spectrally resolved setup inherent to the confocal microscope was used for collecting the backward-generated SHG (BSHG) signals (435 to 440 nm) and the TPEF (450 to 700 nm). The images involved in this study were collected by averaging 3 frames of 512×512 pixels acquired at 200 lines/s. Laser beam powers lower than 15 mW, measured in the objective focus, were used during scanning.

The input excitation laser beam was linearly polarized by a combination between an achromatic quarter-wave plate (AQWP05M-980, Thorlabs) and an achromatic half-wave plate (AHWP05M-980, Thorlabs) mounted in motorized rotation stages (PRM1/MZ8, Thorlabs) and placed in the laser beam path before the microscope. The input laser polarization control followed a procedure similar to [40], resulting in values less than 0.12 for the ellipticity of the linear polarization states. PSHG image stacks were acquired by rotating the linear laser beam polarization by increments of 20° from 0° to 180°. The same quarter-wave plate and half-wave plate combination was used to create a circular polarized laser beam which was used for the SHG intensity estimation.

Biomedical Optics EXPRESS

2.2. Sample preparation

To test the influence of the H&E staining on the SHG emission and PSHG parameter extraction we used skin and breast tissues samples obtained from the Department of Pathology, Bucharest Emergency University Hospital, according to all institutional protocols. All samples were deidentified prior to imaging. The tissue samples were processed according to standard histology procedures, being fixed in formalin (10%), dehydrated through alcohol and xylene passages, and embedded in a block of paraffin wax for slicing by a microtome. Even though a procedure which implies first imaging the unstained section by SHG microscopy, then staining the section and re-imaging the same area might be more straightforward, its implementation raises some practical problems. For example, in our case we have observed that for some tissue areas (e.g., in the case of skin tissue the dermo-epidermal junction and in the case of breast tissue sample areas containing lipids) laser induced damage arises which affects the initial morphology of the samples. Hence, four thin serial sections (2 μm) were cut from the same paraffin-embedded tissue block, mounted on glass slides and de-paraffinized by using alcohol and xylene passages. Two slides were stained with H&E dyes using the standard procedure and covered with coverslips. Two additional control samples were left unstained. One of the H&E-stained tissue section was imaged using a bright-field microscope (Leica DM3000 LED) for reference. Trained pathologists identified according to criteria specific to each tissue type different regions of interest (ROIs) which were further imaged by SHG microscopy on all four tissue slides resulting in four PSHG image stacks per selected ROI. A total of 118 ROIs for skin tissues samples and 98 ROIs for breast tissue samples were imaged and analyzed. Each scanned area size is determined based on previous results [20]. Both the optimal pixel size computed according to the Nyquist criterion and the need to accommodate a larger sample area were considered. According to these criteria, we included in our study ROIs of 125×125 μm^2.

2.3. Image analysis

A custom Matlab code [19] based on the Fourier analysis of the PSHG datasets [16] was used for fitting the PSHG image stacks in a pixel-by-pixel procedure with a theoretical collagen model. The collagen SHG intensity dependence with the input polarization angle can be written as:

$$I_{SHG} = I_0 \cdot \left[sin^2 2(\varphi - \alpha) + \left(\frac{\chi_{31}}{\chi_{15}} \cdot sin^2(\varphi - \alpha) + \frac{\chi_{33}}{\chi_{15}} \cdot cos^2(\varphi - \alpha) \right)^2 \right] \quad (1)$$

where I_0 is a multiplication factor, α is the incident laser beam polarization angle, while φ is the in-plane collagen fiber orientation angle, and χ_{15}, χ_{31}, χ_{33} are the only nonzero elements of the second order susceptibility tensor $\chi^{(2)}$ under the assumption of cylindrical symmetry of collagen.

From the PSHG stacks, each consisting in 10 images, pixel sets with at least seven nonzero values were provided as input to the fitting algorithm. Using this fitting procedure we have computed in a pixel-by-pixel manner two $\chi^{(2)}$ elements ratios (χERs), namely χ_{31}/χ_{15} and χ_{33}/χ_{15} resulting in the χER images. The quality of the fitting procedure was quantified by the coefficient of determination R^2 ($0 < R^2 < 1$), a value closer to unity indicating a better fitting. The coefficient of determination was computed considering that the data are the 10 values for each pixel depending on the input laser polarization (0° to 180° in steps of 20°), while the fitted (predicted) values are those computed with Eq. (1), where χ_{31}/χ_{15}, χ_{33}/χ_{15} and φ are those obtained from the fitting algorithm (Fig. 1(d)). To evaluate the fitting efficiency [20], we computed the ratio between the number of pixels with $R^2 > 0.8$ and the total number of pixels which entered the fitting algorithm. To estimate the SHG intensity we used a circular polarized laser beam and computed the average pixel intensity in the acquired images. SHG images were first thresholded by applying an auto threshold procedure in ImageJ [41], resulting in a collagen mask. The thresholding method was MinError which was chosen after the analysis of the results obtained

Biomedical Optics EXPRESS

with all the available auto thresholding methods in ImageJ. The average pixel intensity was computed for the pixels within the mask.

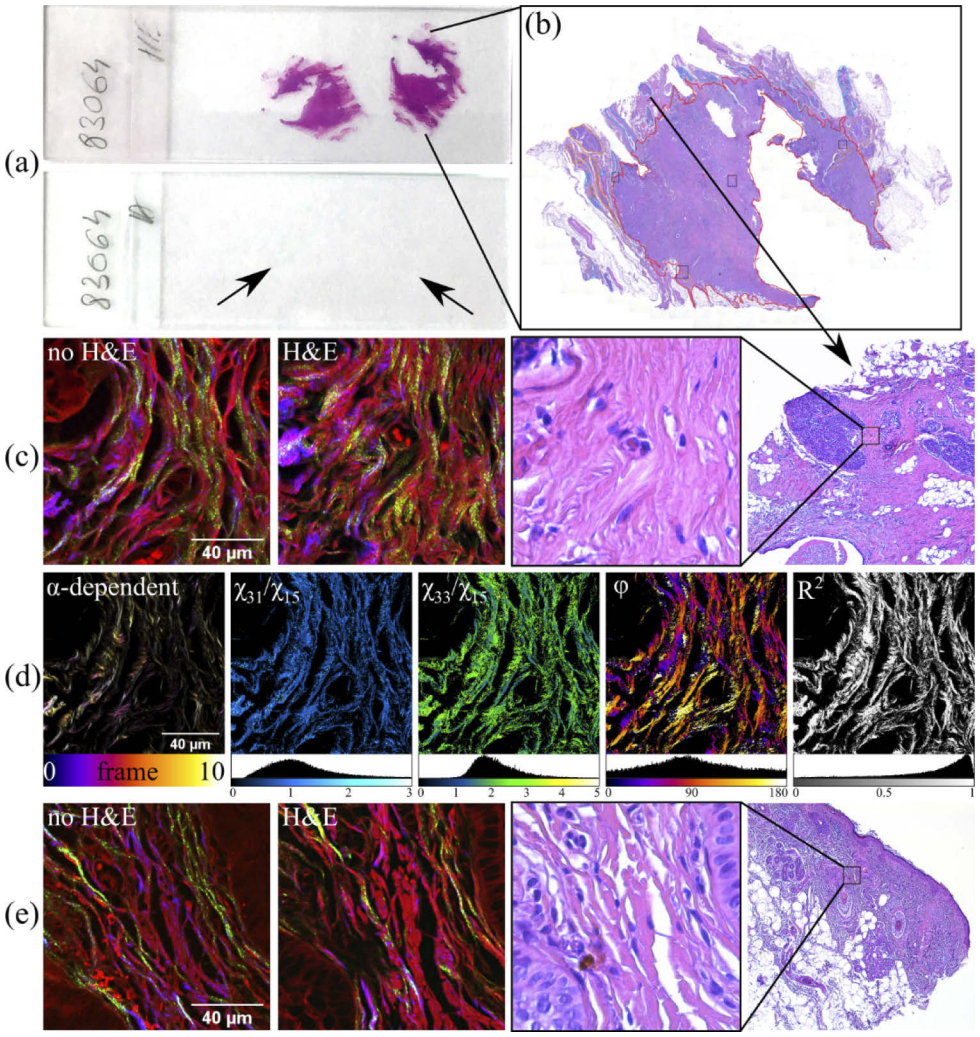

Fig. 1. Schematic representation of the imaging and quantification protocol: (a) images of two histology slides containing serial tissue sections, two stained with H&E (upper slide), and two unstained (lower slide, with the arrows indicating the position of the tissue sections); (b) large image depicting one H&E-stained tissue section; (c) image sets acquired on slides containing breast tissue; (d) polarization angle vs. SHG intensity (color-coded, with frames from 0 to 10 corresponding to polarization angles from 0° to 180° in steps of 20°) and images obtained from the FSHG image set and corresponding histograms; (e) image sets acquired on slides containing epithelial tissue. For (c) and (e) the MPM images are pseudo-colored: blue-color for FSHG, green-color for BSHG and red-color for autofluorescent tissue regions (probed by TPEF).

2.4. *Statistical analysis*

Statistical analysis was performed with Prism 8.4 (GraphPad Software, USA). The D'Agostino & Pearson test was performed to check for normality and depending on the result, either the unpaired

Biomedical Optics EXPRESS

two-tailed t-test or the Mann-Whitney non-parametric test was used, with p values less than 0.05 being considered statistically significant. The one sample t-test or its non-parametric alternative one-sample Wilcoxon signed rank test was used to determine whether the mean/median of the sample is equal to a fixed value.

3. Results

3.1. Nonlinear optical imaging

Four serial tissue sections (Fig. 1(a)) were prepared from the same tissue block with two being H&E stained and two left unstained to investigate the influence of H&E staining on PSHG imaging. Simultaneous images of the sections were collected using BSHG/FSHG and TPEF contrast mechanisms with the nonlinear optical microscope (Fig. 1(c) and (e)).

In Fig. 1 we present a set of MPM images (overlaid TPEF and BSHG/FSHG) of the two tissue types of interest, demonstrating the utility of MPM imaging of both skin and breast tissue in helping the pathologist to assess the tissues state. The MPM images were collected on both H&E-stained and unstained tissue sections, accompanied by bright-field microscopy images collected on the corresponding regions of the H&E-stained tissue section at different magnifications. As expected, the autofluorescence of the unstained samples was weaker than the TPEF intensity of the H&E-stained tissue sections, with the TPEF signal originating in the latter case from the eosin stain highlighting predominantly the connective tissue. The autofluorescence probed by TPEF on unstained tissues showed fibrillar structures as well as some cellular structures, such as cell borders. For observing these details considerable higher excitation powers were used compared to the case of TPEF imaging of H&E-stained tissues. SHG was generated in both forward and backward directions predominantly from collagen. The forward and backward SHG signals provide different, but complementary information about the imaged tissue structure. It is known that observable BSHG signals are comprised of both backscattered FSHG signals and SHG photons directly resulted in the backward direction [42]. In the case of thin tissue slices the effect of backscattering of the forward-generated SHG should be negligible, hence the BSHG in our case entirely consists of backward-generated SHG. While in FSHG images continuous fibrillar collagen structures can be observed, these features are absent in BSHG images where heterogeneous features predominate.

Regarding the breast tissue sample, the wavy appearance of normal collagen fibers in the vicinity of terminal ductal-lobular units (TDLUs) can be seen in Fig. 1(c). A densification of the collagen fibers of the capillary walls can be observed. Fibroblasts can be noticed indirectly; they have nuclei with weak TPEF signals that cause the image of the collagen network to be focally interrupted. The MPM images acquired on the unstained samples denote a similar appearance.

In Fig. 1(e) one can observe a collagen architecture specific to a healthy papillary dermis. The complex network of collagen fibers at this level is intact and has TPEF signals of similar intensity. TPEF signals also indirectly outline the nuclear contour of fibroblasts present in the collagen network and of few keratinocytes of the basal epidermal layer in the lower left and upper right corners of the image. These cells exhibit dim, homogeneous TPEF signals determined by cytokeratins inside the keratinocytes. The main difference between H&E-stained and unstained samples is the higher intensity of TPEF originating from eosin-stained tissue structures (e.g., collagen), which in many cases obstructs the imaging of other tissue structures. The unstained samples offer more details regarding the structure and orientation of the collagen fibers and the adjacent histological elements.

Biomedical Optics EXPRESS

3.2. Parameters analysis

For each imaged ROI we first compute the χER images resulting in the complete image set which is comprised of the PSHG image stack (10 images), the χ_{31}/χ_{15} and χ_{33}/χ_{15} images (Fig. 1(d)). Representative image sets are provided for the skin tissue (Fig. 2) and the breast tissue (Fig. 3).

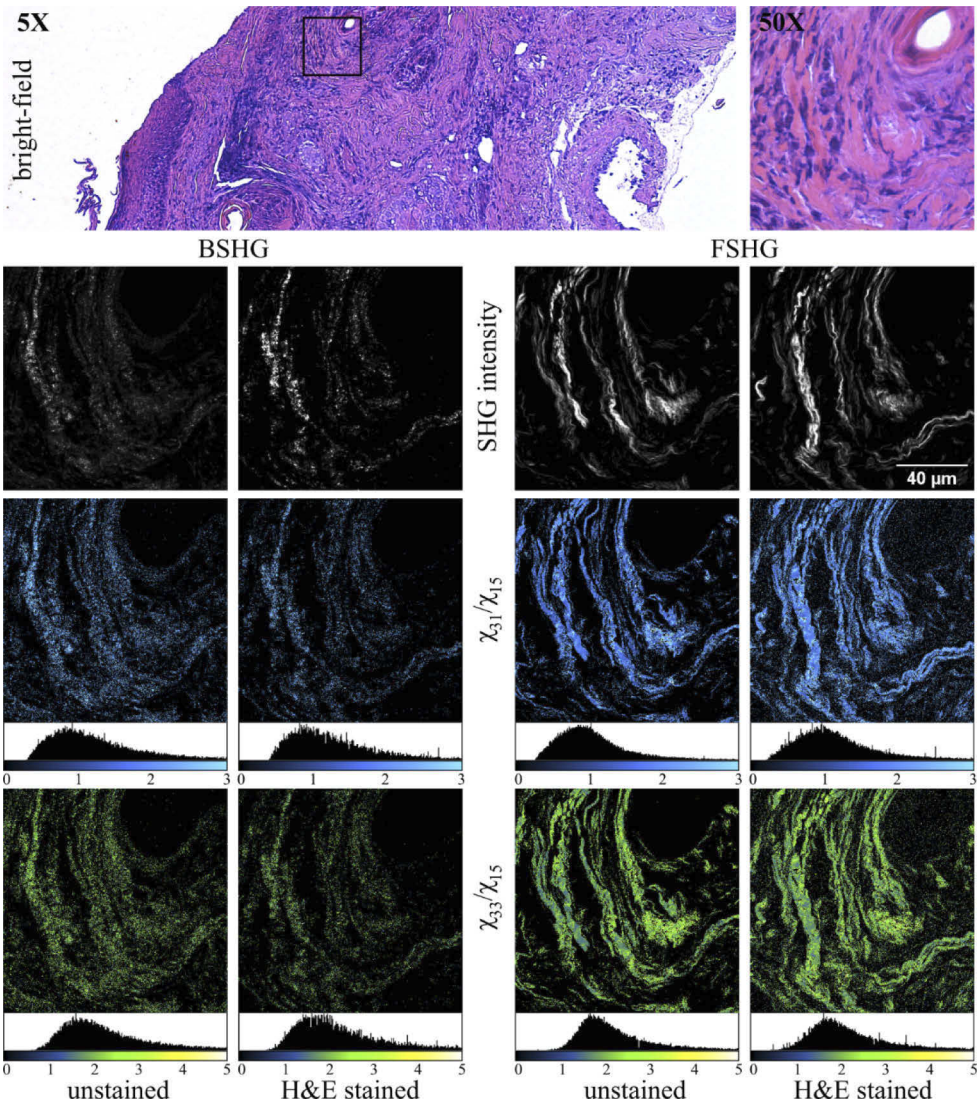

Fig. 2. Complete image set obtained in the case of a skin tissue ROI. The square ROI in the BM image indicates the scanned area of 125×125 μm^2. BSHG and FSHG images are acquired on both unstained and H&E-stained tissue sections. The SHG intensity image is the average of the 10 image PSHG set. χER images (χ_{31}/χ_{15} and χ_{33}/χ_{15}) are computed for each case.

To evaluate the influence of H&E staining on the PSHG imaging and quantitative analysis we compared the values of the following parameters: χERs, the fitting efficiency and the SHG intensity on tissue sections prepared as per standard histology procedure (H&E-stained) and tissue sections following the same procedure but excluding the H&E staining step. The H&E staining influence on the aforementioned parameters was examined on skin and breast tissue

Biomedical Optics EXPRESS

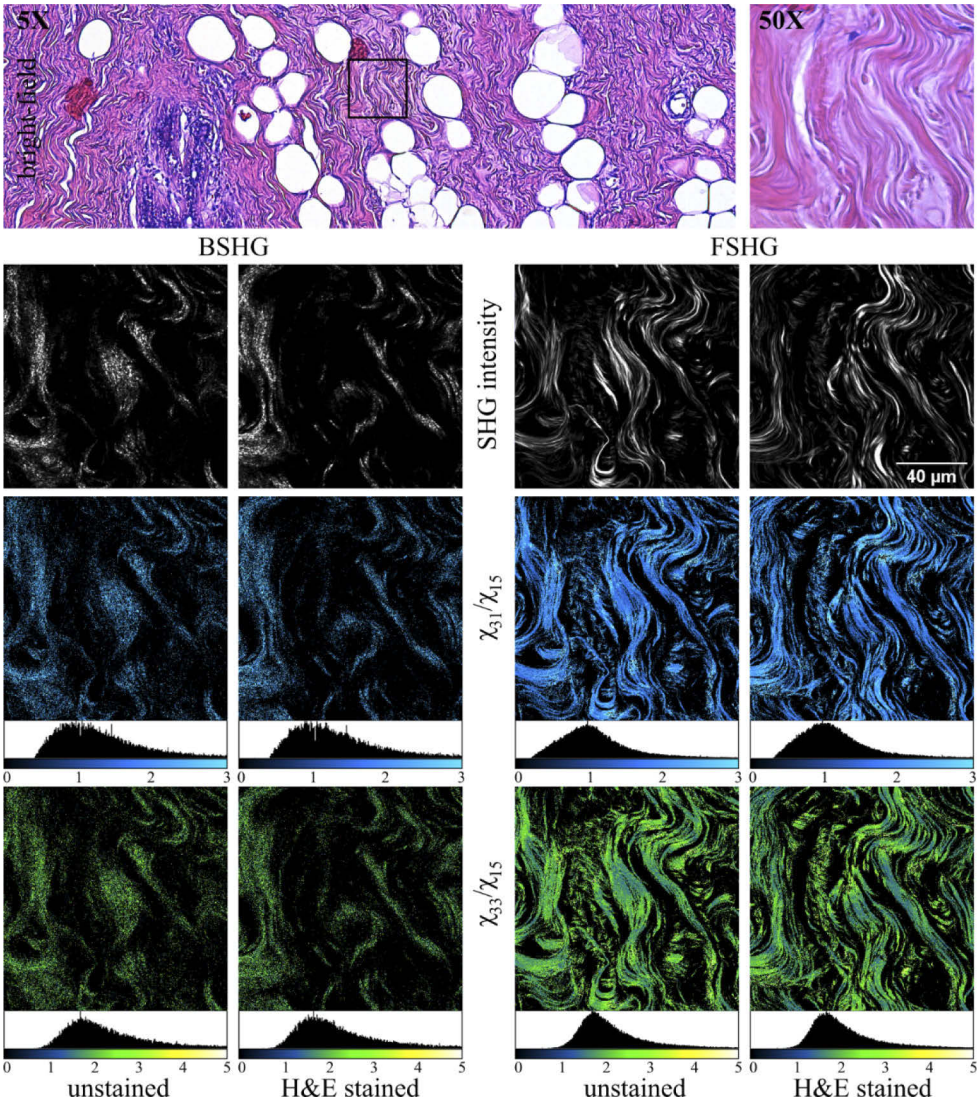

Fig. 3. Complete image set obtained in the case of a breast tissue ROI. The BM images are obtained on one of the H&E-stained tissue sections. BSHG and FSHG images are acquired on both unstained and H&E-stained tissue sections. χER images are computed for each case.

Biomedical Optics EXPRESS

sections with different ROIs selected for imaging on each tissue type. Given the diversity of ROIs, different parameter values were expected, hence when determining the influence of the H&E staining, we compared not the actual parameter values but its relative change from the unstained tissue section to the H&E-stained tissue section.

For each parameter we computed the relative inherent variability which is due to the sample preparation, the imaging setup, and the fitting procedure. For this we compared the relative change of the parameters of interest between serial tissue sections either H&E-stained or unstained. We assumed that small changes between serial sections in terms of tissue architecture translate in small variations in parameter values between sections. In such cases either the Mann-Whitney test or the t test did not reveal any statistically significant differences between slides. This situation was considered as a class of ROIs for which the relative change of a parameter is only due to inherent system limitations. On the other hand, for several serial sections tissue architecture artefacts were visible on the prepared slides possibly due to mishandling the tissue section. These artefacts translated into a significant variation in parameters between slides. This was considered as the class of ROIs for which a real relative change between serial sections was obtained. For each individual parameter we performed a receiver operating characteristic (ROC) analysis and determined the optimal cutoff value between the two classes based on the Youden index. When comparing H&E-stained with unstained tissue sections, a constant parameter (variations only to inherent imaging and fitting limitations) was inferred when a relative parameter change below the threshold was obtained. Meaningful variations either positive or negative, were considered in situations when the absolute relative change was above the computed threshold value.

3.2.1. Second order susceptibility tensor elements ratios

For the case of FSHG images the ROC analysis returned a value of the inherent inter-section variability of 3.9% (χ_{31}/χ_{15}) and 2.7% (χ_{33}/χ_{15}) for skin tissue samples and of 5.1% (χ_{31}/χ_{15}) and 3.4% (χ_{33}/χ_{15}) for the breast tissue samples, respectively. By using these threshold values the χERs behavior with H&E staining is summarized in Table 1.

Table 1. Percent of ROIs with their relative change for χERs from the unstained to H&E-stained tissue sections for FSHG datasets.

Relative change	Skin tissue sections		Breast tissue sections	
	χ_{31}/χ_{15}	χ_{33}/χ_{15}	χ_{31}/χ_{15}	χ_{33}/χ_{15}
Increase	69%	61%	4%	8%
Decrease	11%	17%	67%	57%
Constant	20%	22%	29%	35%

By applying a Wilcoxon one sample test on the skin tissue dataset, median increases of 8.5% for χ_{31}/χ_{15} ($p < 0.0001$) and of 3.8% for χ_{33}/χ_{15} ($p = 0.0001$) were obtained. Both these values are above the threshold values for intrinsic variability. On the other hand, the same statistical test applied on the breast tissue datasets revealed median decreases after H&E staining of 8.3% for χ_{31}/χ_{15} ($p < 0.0001$) and of 3.9% for χ_{33}/χ_{15} ($p < 0.0001$). Both these values are again above the threshold values for intrinsic variability obtained for the breast tissue images.

For the case of BSHG images the ROC analysis returned a value of the inherent inter-section variability of 4.6% (χ_{31}/χ_{15}) and 3.4% (χ_{33}/χ_{15}) for skin tissue samples and of 9.2% (χ_{31}/χ_{15}) and 5.1% (χ_{33}/χ_{15}) for the breast tissue samples, respectively. By using these threshold values the χERs behavior with H&E staining is summarized in Table 2.

By applying a Wilcoxon one sample test on the skin tissue dataset, median increases of 3.5% for χ_{31}/χ_{15} ($p < 0.0001$) and of 0.02% for χ_{33}/χ_{15} ($p = 0.69$) were obtained. Both these values are under the threshold values for intrinsic variability. The same statistical test applied on the breast tissue datasets revealed median decreases after H&E staining with 8.1% for χ_{31}/χ_{15} ($p < 0.0001$)

Biomedical Optics EXPRESS

Table 2. Percent of ROIs with their relative change for χERs from the unstained to H&E-stained tissue sections for BSHG datasets

Relative change	Skin tissue sections		Breast tissue sections	
	χ_{31}/χ_{15}	χ_{33}/χ_{15}	χ_{31}/χ_{15}	χ_{33}/χ_{15}
Increase	45%	32%	3%	0%
Decrease	5%	26%	46%	31%
Constant	50%	42%	51%	69%

and of 2.2% for χ_{33}/χ_{15} ($p < 0.0001$). Both these values are again under the threshold values for intrinsic variability obtained for the breast tissue images. The results obtained for the χERs variation in BSHG imaging are thus inconclusive.

3.2.2. Fitting efficiency

For the case of FSHG images the ROC analysis returned a value of the inherent inter-section variability for the fitting efficiency of 6% for skin tissue samples and of 8.1% for the breast tissue samples, respectively. By using these threshold values the fitting efficiency behavior with H&E staining is summarized in Table 3.

Table 3. Percent of ROIs with their relative change of the fitting efficiency from the unstained to H&E-stained tissue sections for FSHG datasets.

Relative change	Skin tissue sections	Breast tissue sections
Increase	18%	6%
Decrease	57%	29%
Constant	25%	65%

By applying a Wilcoxon one sample test on the skin tissue datasets a median decrease with H&E staining of 15.4% ($p < 0.0001$) was obtained in the case of the fitting efficiency. The value is greater than the intrinsic variability threshold. On the other hand, the same statistical test applied on the breast tissue datasets revealed a median decrease after H&E staining of only 4.9% ($p = 0.0004$), a value which is under the threshold.

For the case of BSHG images the ROC analysis returned a value of the inherent inter-section variability for the fitting efficiency of 23.7% for skin tissue samples and of 22% for the breast tissue samples, respectively. By using these threshold values the fitting efficiency behavior with H&E staining is summarized in Table 4.

Table 4. Percent of ROIs with their relative change of the fitting efficiency from the unstained to H&E-stained tissue sections for BSHG datasets.

Relative change	Skin tissue sections	Breast tissue sections
Increase	0%	0%
Decrease	87%	85%
Constant	13%	15%

By applying a Wilcoxon one sample test on the skin tissue datasets a median decrease with H&E staining of 38% ($p < 0.0001$) was obtained in the case of the fitting efficiency. The value is greater than the intrinsic variability threshold. On the other hand, the same statistical test applied on the breast tissue datasets revealed a median decrease after H&E staining of 43% ($p < 0.0001$), a value which is again greater than the threshold.

Biomedical Optics EXPRESS

3.2.3. Average pixel intensity

For the case of FSHG images the ROC analysis returned an inherent inter-section variability for the average pixel intensity of 23.4% and 13.1% for skin tissue and breast tissue samples, respectively. Using these threshold values the average pixel intensity behavior with H&E staining for circular polarization is summarized in Table 5.

Table 5. Percent of ROIs with their relative change of the average pixel intensity in FSHG images from unstained to H&E-stained tissue sections.

Relative change	Skin tissue sections	Breast tissue sections
Increase	7%	4%
Decrease	59%	25%
Constant	34%	71%

By applying a Wilcoxon one sample test on the skin tissue datasets, a median decrease of 26% ($p = 0.0001$) was obtained, which is above the inter-section variability threshold. On the other hand, the same statistical test applied on the breast tissue datasets revealed a median decrease after H&E staining of 5.9% ($p < 0.0001$). Even though the average pixel intensity has a statistically significant decrease, the value is below the threshold.

For the case of BSHG images the ROC analysis returned a value of the inherent inter-section variability of 31.8% for skin tissue samples and of 17.2% for the breast tissue samples, respectively. These threshold values were used to assess the average pixel intensity behavior with H&E staining. The results are summarized in Table 6.

Table 6. Percent of ROIs with their relative change of the average pixel intensity in BSHG images from the unstained to H&E-stained tissue sections.

Relative change	Skin tissue sections	Breast tissue sections
Increase	0%	3%
Decrease	53%	85%
Constant	48%	12%

By applying a Wilcoxon one sample test on the skin tissue datasets, a median decrease of 41% ($p = 0.0001$) was obtained. The value is above the inter-section variability threshold. On the other hand, the same statistical test applied on the breast tissue datasets revealed a median decrease after H&E staining of 38% ($p < 0.0001$) a value which is again above the threshold for intrinsic variability.

4. Discussions

Nonlinear optical imaging techniques are becoming established as very powerful tissue characterization tools whose demonstrated roles in complementing traditional histopathology protocols is very important to consider in the quest for faster and better diagnostics. Their intrinsic contrast mechanisms that allow label-free probing of tissue samples to result in images that recapitulate the most important morphological features that expert pathologists look for to assess the tissue state are available for in vivo, ex vivo and fixed tissues. In our study, we focus on SHG imaging of fixed tissue sections both unstained and H&E-stained, following the classical histological protocol. The aim was to assess the influence of H&E staining on the extraction of quantitative image parameters specific to PSHG tissue imaging. Our results indicate a modification of less than 10% for the χERs after H&E staining for both skin and breast tissue samples. It is noteworthy to mention that if in the case of skin tissue samples, the χER values increased after

Biomedical Optics EXPRESS

H&E staining, for breast tissues, the results indicate a decrease of both computed χERs. Although the results were statistically relevant, we would like to point out that the statistical tests in the case of χERs were conducted on pixel sets extracted from the χER images containing 10000 pixels with $R^2 > 0.8$. Performing statistical analysis on such extended datasets might eventually provide statistical relevant differences. In these cases, depending on pathology or the tissue under investigation small differences in χERs might be or not relevant for the actual experiment. On the other hand, the collagen networks in skin and breast tissues have different architectures, as previously demonstrated. Normal breast tissue has a wavy collagen pattern, which transforms into linear strands of collagen parallel to the breast tumor in case of malignancy [43]. In the case of skin tissue, collagen has a higher orientation index indicating parallel fibers close to the epidermis, with the index decreasing for collagen bundles in deeper skin layers [44]. Hence different collagen architectures yield different behavior when the tissue is H&E-stained compared to the fixed, unstained tissue. Further investigation might be necessary on different tissue types and/or pathologies to draw a conclusion.

The fitting efficiency dropped as much as ~43% for BSHG images and to a lower degree (< 15%) for FSHG images. Fitting efficiency accounts for a change in the collagen fibril structure but also on changes in the collection pathway, which in this case is influenced by the H&E staining. While the former can be probed by looking at the χERs results, for the latter information may be found in the SHG intensity behavior with the H&E staining which we have estimated by calculating the average pixel intensity. Because for χERs only small variations were obtained, we estimate that the change in fitting efficiency can be explained by the SHG intensity modification which is discussed in the following.

In the SHG images acquires under circular polarization, the average pixel intensity has dropped ~40% after H&E staining in BSHG images acquired on both tissue types. For FSHG images the results indicate a decrease of ~25% for skin tissue, while in the case of the breast tissue samples there was no statistically relevant change in the FSHG intensity. Because the results in the case of FSHG images differ between skin and breast tissue samples we also computed the forward-to-backward SHG (F/B) ratio change after H&E staining and obtained a decrease of 15% and 27% in the case of skin and breast tissue samples, respectively. It has been previously reported that the F/B ratio might be indicative for the axial size of the scatterer within the focal volume [14] (e.g., collagen fibrils of different age have different thicknesses and thus translate in a local change of the F/B ratio). Moreover, Williams et. al. [14] report a decrease of the F/B ratio in the case of paraformaldehyde-fixed collagenous samples under saline solution treatment which can be estimated to ~20%. A similar explanation for the F/B decrease can be considered in the case of H&E staining, that is a change in the collagen fibril shell from where the SH is generated.

A decrease in SHG intensity does not have an impact on the quantitative analysis of PSHG datasets and eventually can be compensated by an increase of laser power or pixel dwell time, if necessary, for a subjective analysis of the SHG images. On the other hand, the decrease in efficiency especially on the BSHG channel might have an impact on the number of relevant pixels (e.g., with $R^2 > 0.8$) which might be used for the statistical analysis of the PSHG datasets. If both BSHG and FSHG channels are acquired, this loss in intensity can be compensated by the possibility of computing the F/B ratio to provide additional information. Another advantage of using H&E-stained tissue sections especially in microscopy setups ready to acquire third harmonic generation images, which can be straightforward to accomplish in a MPM setup with SHG/TPEF capabilities is the enhancement of nuclear structures in THG imaging under H&E staining [34]. On the other hand, a drawback of using H&E-stained tissue section is the hindering of the autofluorescence probed by TPEF which in some experiments can be used to complement the analysis of PSHG datasets [8].

We evaluated the influence of the hematoxylin and eosin staining on the extraction of quantitative image parameters that describe the collagen structure, specific to image datasets obtained by

Biomedical Optics EXPRESS

polarization-resolved SHG microscopy. Thin serial tissue sections prepared as per standard histology protocol and stained with hematoxylin and eosin as well as their unstained pairs from skin and breast tissue samples were imaged. A fitting algorithm which provides ratios of the second order susceptibility tensor elements, fitting efficiency and average pixel intensities were assessed. While in the case of the susceptibility tensor elements ratios the change was inconclusive for the two tissue types which were under study, both the fitting efficiency and the average pixel intensity had a significant decrease for H&E-stained tissues, especially on the backward SHG pathway. By computing the forward-to-backward SHG ratio the influence of H&E staining on the collagen was connected to a possible modification in the SH-generating collagen shell. Our results show thus that similar quantitative analysis workflows applied to PSHG images collected on stained and unstained tissues yield different results, which can hinder the diagnostic accuracy if applied in an unsupervised manner. These findings suggest the need for novel PSHG image analysis methods and workflows that are specifically dedicate to stained or unstained tissue, and of methods that are capable to generalize better than current ones. Although our current results provide interesting findings on the influence of the H&E staining on the extraction of quantitative image parameters that describe the collagen structure, future experiments might shed more light on aspects which were currently inconclusive. Such future experiments might consider different collagen models (e.g., the generic model), different tissue types, or even different laser wavelengths.

Funding. European Regional Development Fund (MySMIS code 107066, P_36_611); Unitatea Executiva pentru Finantarea Invatamantului Superior, a Cercetarii, Dezvoltarii si Inovarii (PN-III-P1-1.1-TE-2019-1756, PN-III-P2-2.1-PED-2019-1666).

Acknowledgments. This work was supported by the Romanian Executive Agency for Higher Education, Research, Development and Innovation Funding (UEFISCDI) under grants PN-III-P1-1.1-TE-2019-1756 (SHGThyPath) [RH, BP, GAS] and PN-III-P2-2.1-PED-2019-1666 (GastroDeep) [SGS, AD, IF, MC]. The use of the Ti:Sapphire laser (Chameleon Ultra II, Coherent) was possible due to European Regional Development Fund through Competitiveness Operational Program 2014-2020, Priority axis 1, Project No. P_36_611, MySMIS code 107066, Innovative Technologies for Materials Quality Assurance in Health, Energy and Environmental - Center for Innovative Manufacturing Solutions of Smart Biomaterials and Biomedical Surfaces – INOVABIOMED.

Disclosures. The authors declare no competing interests.

Data availability. Data underlying the results presented in this paper are not publicly available at this time but may be obtained from the authors upon reasonable request.

References

1. J. A. Kiernan, *Histological and Histochemical Methods* (Oxford University Press, 1999).
2. W. R. Zipfel, R. M. Williams, and W. W. Webb, "Nonlinear magic: multiphoton microscopy in the biosciences," Nat. Biotechnol. **21**(11), 1369–1377 (2003).
3. A. Dilipkumar, A. Al-Shemmary, L. Kreiß, K. Cvecek, B. Carlé, F. Knieling, J. Gonzales Menezes, O. M. Thoma, M. Schmidt, M. F. Neurath, M. Waldner, O. Friedrich, and S. Schürmann, "Label-free multiphoton endomicroscopy for minimally invasive in vivo imaging," Adv. Sci. **6**(8), 1801735 (2019).
4. M. Balu, C. B. Zachary, R. M. Harris, T. B. Krasieva, K. König, B. J. Tromberg, and K. M. Kelly, "In vivo multiphoton microscopy of basal cell carcinoma," JAMA Dermatol. **151**(10), 1068–1074 (2015).
5. J. N. Rogart, J. Nagata, C. S. Loeser, R. D. Roorda, H. Aslanian, M. E. Robert, W. R. Zipfel, and M. H. Nathanson, "Multiphoton imaging can be used for microscopic examination of intact human gastrointestinal mucosa ex vivo," Clin. Gastroenterol. Hepatol. **6**(1), 95–101 (2008).
6. S. W. Perry, R. M. Burke, and E. B. Brown, "Two-photon and second harmonic microscopy in clinical and translational cancer research," Ann. Biomed. Eng. **40**(2), 277–291 (2012).
7. T. Makino, M. Jain, D. C. Montrose, A. Aggarwal, J. Sterling, B. P. Bosworth, J. W. Milsom, B. D. Robinson, M. M. Shevchuk, K. Kawaguchi, N. Zhang, C. M. Brown, D. R. Rivera, W. O. Williams, C. Xu, A. J. Dannenberg, and S. Mukherjee, "Multiphoton tomographic imaging: A potential optical biopsy tool for detecting gastrointestinal inflammation and neoplasia," Cancer Prev. Res. **5**(11), 1280–1290 (2012).
8. M. J. Huttunen, R. Hristu, A. Dumitru, I. Floroiu, M. Costache, and S. G. Stanciu, "Multiphoton microscopy of the dermoepidermal junction and automated identification of dysplastic tissues with deep learning," Biomed. Opt. Express **11**(1), 186–199 (2020).
9. W. Denk, J. H. Strickler, and W. W. Webb, "Two-photon laser scanning fluorescence microscopy," Science **248**(4951), 73–76 (1990).

Biomedical Optics EXPRESS

10. T. B. Krasieva, C. Stringari, F. Liu, C.-H. Sun, Y. Kong, M. Balu, F. L. Meyskens, E. Gratton, and B. J. Tromberg, "Two-photon excited fluorescence lifetime imaging and spectroscopy of melanins in vitro and in vivo," J. Biomed. Opt. **18**(3), 031107 (2013).
11. Z. Liu, D. Pouli, C. A. Alonzo, A. Varone, S. Karaliota, K. P. Quinn, K. Mönger, K. P. Karalis, and I. Georgakoudi, "Mapping metabolic changes by noninvasive, multiparametric, high-resolution imaging using endogenous contrast," Sci. Adv. **4**(3), eaap9302 (2018).
12. V. Van Steenbergen, W. Boesmans, Z. Li, Y. de Coene, K. Vints, P. Baatsen, I. Dewachter, M. Ameloot, K. Clays, and P. Vanden Berghe, "Molecular understanding of label-free second harmonic imaging of microtubules," Nat. Commun. **10**(1), 3530 (2019).
13. S. V Plotnikov, A. C. Millard, P. J. Campagnola, and W. A. Mohler, "Characterization of the myosin-based source for second-harmonic generation from muscle sarcomeres," Biophys. J. **90**(2), 693–703 (2006).
14. R. M. Williams, W. R. Zipfel, and W. W. Webb, "Interpreting second-harmonic generation images of collagen I fibrils," Biophys. J. **88**(2), 1377–1386 (2005).
15. X. Chen, O. Nadiarynkh, S. Plotnikov, and P. J. Campagnola, "Second harmonic generation microscopy for quantitative analysis of collagen fibrillar structure," Nat. Protoc. **7**(4), 654–669 (2012).
16. I. Amat-Roldan, S. Psilodimitrakopoulos, P. Loza-Alvarez, and D. Artigas, "Fast image analysis in polarization SHG microscopy," Opt. Express **18**(16), 17209–17219 (2010).
17. C.-H. Chen, A. V. Nair, S.-C. Chuang, Y.-S. Lin, M.-H. Cheng, C.-Y. Lin, C.-Y. Chang, S.-J. Chen, and C.-H. Lien, "Dual-LC PSHG microscopy for imaging collagen type I and type II gels with pixel-resolution analysis," Biomed. Opt. Express **12**(5), 3050–3065 (2021).
18. R. Hristu, L. G. Eftimie, B. Paun, S. G. Stanciu, and G. A. Stanciu, "Pixel-level angular quantification of capsular collagen in second harmonic generation microscopy images of encapsulated thyroid nodules," J. Biophotonics **13**(12), e202000262 (2020).
19. S. Psilodimitrakopoulos, P. Loza-Alvarez, and D. Artigas, "Fast monitoring of in-vivo conformational changes in myosin using single scan polarization-SHG microscopy," Biomed. Opt. Express **5**(12), 4362–4373 (2014).
20. B. Paun, R. Hristu, S. G. Stanciu, A. V. Dumitru, M. Costache, and G. A. Stanciu, "Strategies for optimizing the determination of second-order nonlinear susceptibility tensor coefficients for collagen in histological samples," IEEE Access **7**, 135210–135219 (2019).
21. R. Hristu, L. G. Eftimie, S. G. Stanciu, D. E. Tranca, B. Paun, M. Sajin, and G. A. Stanciu, "Quantitative second harmonic generation microscopy for the structural characterization of capsular collagen in thyroid neoplasms," Biomed. Opt. Express **9**(8), 3923–3936 (2018).
22. R. Cicchi, D. Kapsokalyvas, and F. S. Pavone, "Clinical nonlinear laser imaging of human skin: a review," *Biomed Res. Int*. (2014).
23. A. Golaraei, L. Kontenis, R. Cisek, D. Tokarz, S. J. Done, B. C. Wilson, and V. Barzda, "Changes of collagen ultrastructure in breast cancer tissue determined by second-harmonic generation double Stokes-Mueller polarimetric microscopy," Biomed. Opt. Express **7**(10), 4054–4068 (2016).
24. K. Tilbury and P. J. Campagnola, "Applications of second-harmonic generation imaging microscopy in ovarian and breast cancer," Perspect Medicin Chem **7**, PMC.S13214 (2015).
25. J. Adur, V. B. Pelegati, A. A. de Thomaz, M. O. Baratti, L. A. L. A. Andrade, H. F. Carvalho, F. Bottcher-Luiz, and C. L. Cesar, "Second harmonic generation microscopy as a powerful diagnostic imaging modality for human ovarian cancer," J. Biophotonics **7**(1-2), 37–48 (2014).
26. D. Tokarz, R. Cisek, A. Joseph, S. L. Asa, B. C. Wilson, and V. Barzda, "Characterization of pathological thyroid tissue using polarization-sensitive second harmonic generation microscopy," Lab Invest **100**(10), 1280–1287 (2020).
27. D. Tokarz, R. Cisek, A. Joseph, A. Golaraei, K. Mirsanaye, S. Krouglov, S. L. Asa, B. C. Wilson, and V. Barzda, "Characterization of pancreatic cancer tissue using multiphoton excitation fluorescence and polarization-sensitive harmonic generation microscopy," Front. Oncol. **9**, 272 (2019).
28. B. K. Robinson, E. Cortes, A. J. Rice, M. Sarper, and A. D. R. Hernañdez, "Quantitative analysis of 3D extracellular matrix remodelling by pancreatic stellate cells," Biol. Open **5**(6), 875–882 (2016).
29. B. Sarri, R. Canonge, X. Audier, E. Simon, J. Wojak, F. Caillol, C. Cador, D. Marguet, F. Poizat, M. Giovannini, and H. Rigneault, "Fast stimulated Raman and second harmonic generation imaging for intraoperative gastro-intestinal cancer detection," Sci. Rep. **9**(1), 10052–10 (2019).
30. J. W. Birk, M. Tadros, K. Moezardalan, O. Nadyarnykh, F. Forouhar, J. Anderson, and P. Campagnola, "Second harmonic generation imaging distinguishes both high-grade dysplasia and cancer from normal colonic mucosa," Dig. Dis. Sci. **59**(7), 1529–1534 (2014).
31. R. M. Martínez-Ojeda, M. D. Pérez-Cárceles, L. C. Ardelean, S. G. Stanciu, and J. M. Bueno, "Multiphoton microscopy of oral tissues: review," Front. Phys. **8**, 128 (2020).
32. T. W. Bocklitz, F. S. Salah, N. Vogler, S. Heuke, O. Chernavskaia, C. Schmidt, M. J. Waldner, F. R. Greten, R. Bräuer, M. Schmitt, A. Stallmach, I. Petersen, and J. Popp, "Pseudo-HE images derived from CARS/TPEF/SHG multimodal imaging in combination with Raman-spectroscopy as a pathological screening tool," BMC Cancer **16**(1), 534 (2016).
33. R. A. Natal, J. Vassallo, G. R. Paiva, V. B. Pelegati, G. O. Barbosa, G. R. Mendonça, C. Bondarik, S. F. Derchain, H. F. Carvalho, C. S. Lima, C. L. Cesar, and L. O. Sarian, "Collagen analysis by second-harmonic generation microscopy predicts outcome of luminal breast cancer," Tumor Biol. **40**(4), 101042831877095 (2018).

Biomedical Optics EXPRESS

34. A. Tuer, D. Tokarz, N. Prent, R. Cisek, J. Alami, D. J. Dumont, L. Bakueva, J. Rowlands, and V. Barzda, "Nonlinear multicontrast microscopy of hematoxylin-and-eosin-stained histological sections," J. Biomed. Opt. **15**(2), 026018 (2010).
35. R. Hristu, S. G. Stanciu, D. E. Tranca, and G. A. Stanciu, "Improved quantification of collagen anisotropy with polarization-resolved second harmonic generation microscopy," J. Biophotonics **10**(9), 1171–1179 (2017).
36. J. Chen, J. Xu, D. Kang, M. Xu, S. Zhuo, X. Zhu, and X. Jiang, "Multiphoton microscopic imaging of histological sections without hematoxylin and eosin staining differentiates carcinoma in situ lesion from normal oesophagus," Appl. Phys. Lett. **103**(18), 183701 (2013).
37. Z. Hong, Y. Chen, J. Chen, H. Chen, Y. Xu, X. Zhu, S. Zhuo, Z. Shi, and J. Chen, "Optical diagnosis of gallbladder cancers via two-photon excited fluorescence imaging of unstained histological sections," Lasers Med. Sci. **30**(1), 225–233 (2015).
38. Y. Chen, J. Chen, H. Chen, Z. Hong, X. Zhu, S. Zhuo, Y. Chen, and J. Chen, "Multiphoton microscopy as a diagnostic imaging modality for pancreatic neoplasms without hematoxylin and eosin stains," J. Biomed. Opt. **19**(9), 096008 (2014).
39. M. G. Monaghan, S. Kroll, S. Y. Brucker, and K. Schenke-Layland, "Enabling multiphoton and second harmonic generation imaging in paraffin-embedded and histologically stained sections," Tissue Engineering Part C: Methods **22**(6), 517–523 (2016).
40. E. I. Romijn, A. Finnøy, R. Kumar, and M. B. Lilledahl, "Automated calibration and control for polarization-resolved second harmonic generation on commercial microscopes," PLoS One **13**(4), e0195027 (2018).
41. C. A. Schneider, W. S. Rasband, and K. W. Eliceiri, "NIH Image to ImageJ: 25 years of image analysis," Nat. Methods **9**(7), 671–675 (2012).
42. A. Diaspro and P. Bianchini, "Three-dimensional (3D) backward and forward second harmonic generation (SHG) microscopy of biological tissues," J. Biophotonics **1**(6), 443–450 (2008).
43. E. A. Brett, M. A. Sauter, H.-G. Machens, and D. Duscher, "Tumor-associated collagen signatures: pushing tumor boundaries," Cancer Metab **8**(1), 14 (2020).
44. P. P. M. Van Zuijlen, J. J. B. Ruurda, H. A. Van Veen, J. Van Marle, A. J. M. Van Trier, F. Groenevelt, R. W. Kreis, and E. Middelkoop, "Collagen morphology in human skin and scar tissue: No adaptations in response to mechanical loading at joints," Burns **29**(5), 423–431 (2003).